

# Binary nucleation kinetics. III. Transient behavior and time lags

Barbara E. Wyslouzil

Department of Chemical Engineering, Worcester Polytechnic Institute, Worcester, Massachusetts 01609-2280

Gerald Wilemski

Lawrence Livermore National Laboratory, Livermore, California 94551-9900

(Received 1 February 1996; accepted 9 April 1996)

Transient binary nucleation is more complex than unary because of the bidimensionality of the cluster formation kinetics. To investigate this problem qualitatively and quantitatively, we numerically solved the birth–death equations for vapor-to-liquid phase transitions. Our previous work [J. Chem. Phys. **103**, 1137 (1995)] showed that the customary saddle point and growth path approximations are almost always valid in steady state gas phase nucleation and only fail if the nucleated solution phase is significantly nonideal. The current work demonstrates that in its early transient stages, binary nucleation rarely, if ever, occurs via the saddle point. This affects not only the number of particles forming but their composition and may be important for nucleation in glasses and other condensed mixtures for which time scales are very long. Before reaching the state of saddle point nucleation, most binary systems pass through a temporary stage in which the region of maximum flux extends over a ridge on the free energy surface. When ridge crossing nucleation is the steady state solution, it thus arises quite naturally as an arrested intermediate state that normally occurs in the development of saddle point nucleation. While the time dependent and steady state distributions of the fluxes and concentrations for each binary system are strongly influenced by the gas composition and species impingement rates, the ratio of nonequilibrium to equilibrium concentrations has a quasiuniversal behavior that is determined primarily by the thermodynamic properties of the liquid mixture. To test our quantitative understanding of the transient behavior, we directly calculated the time lag for the saddle point flux and compared it with the available analytical predictions. Although the analytical results overestimate the time lag by factors of 1.2–5, they should be adequate for purposes of planning experiments. We also found that the behavior of the saddle point time lag can indicate when steady state ridge crossing nucleation will occur. © 1996 American Institute of Physics. [S0021-9606(96)01327-X]

## I. INTRODUCTION

During transient binary nucleation, both the number and composition of particles being formed differ from one's expectations based on steady state nucleation. For nucleation in glasses, the time to reach steady state is long, and transient behavior must be considered when interpreting experimental results for phase transformation kinetics.<sup>1,2</sup> In nucleation from the vapor phase, transient effects can be important for experiments with short time scales, for example, in expansion cloud chambers, shock tubes and supersonic nozzle expansions. To determine when transient effects will dominate, we may estimate the time lag for the system. In a time dependent nucleation process, if  $n_g(t)$  is the cumulative number of particles of size  $g$  formed in the time interval  $[0, t]$  and  $J_s$  is the steady state nucleation rate, the time lag  $t_g$  is the parameter that makes the equation (cf. Ref. 3),

$$n_g(t) = J_s \times (t - t_g), \quad (1)$$

asymptotically correct for  $t \gg t_g$ . In general,  $t_g$  depends on the cluster size of interest. In this paper, we restrict consideration to the time lag for the critical cluster size, which will simply be denoted as  $t^*$ .

Considerable effort has been made to understand the behavior of time lags and transient nucleation kinetics in unary

systems.<sup>1–29</sup> In contrast, work on binary systems has been limited, possibly because the two-dimensional nature of cluster formation complicates mathematical analysis. One particular complication not present for unary kinetics is the difficulty in defining the average path followed by a cluster as it grows to critical size and composition. Wilemski<sup>30</sup> developed the first expression for the time lag in binary nucleation by assuming that the major flux through the subcritical cluster sizes followed the path defined by  $\tan \theta = j^*/i^*$ , where  $i^*$  and  $j^*$  are the numbers of  $A$  and  $B$  molecules, respectively, in the critical cluster. He applied his results to estimate  $t^*$  for vapor-to-liquid nucleation in the water–ethanol system and found that when both species are abundant and have vapor phase activities greater than 1, time lags are on the order of 1  $\mu$ s. When the ethanol activity drops below 0.01, the time lag for binary nucleation increases rapidly and homogeneous nucleation of water becomes the only viable nucleation process.

Schelling and Reiss<sup>31</sup> used a variational technique to calculate time lags in the  $\text{H}_2\text{SO}_4$ – $\text{H}_2\text{O}$  system. They found that, under conditions typical of their experiments, the times required to establish the steady state cluster distribution could be on the order of 0.1 s and that even longer times were required for the newly formed particles to grow to an observable size.<sup>32</sup> This theoretical work helped explain their experi-

mental observations<sup>32</sup> that particle formation above  $\text{H}_2\text{SO}_4\text{-H}_2\text{O}$  solutions in an expansion cloud chamber was consistent with either unary nucleation of water or some combination of pure water nucleation and binary nucleation of acidic droplets. Shi and Seinfeld<sup>33</sup> used the method of matched asymptotic expansions to develop expressions for the time dependent rate and the time lag of binary nucleation. They stated that large time lags could be due to anisotropy of the free energy surface as well as to large differences in the impingement rates of the two condensible species. Recently, McGraw<sup>34</sup> used a computational approach based on the negative eigenvalue theorem to obtain the cumulative eigenvalue distribution for nucleation in the  $\text{H}_2\text{SO}_4\text{-H}_2\text{O}$  system. From the smallest eigenvalues he estimated the nucleation time lags and found them to be of the same order of magnitude as those obtained by Schelling and Reiss.<sup>31</sup>

In the second paper (WWII)<sup>35</sup> of this series, we presented steady state results based on our numerical solutions of the binary kinetics equations. In this paper we discuss our transient results. Several other numerical studies of transient binary nucleation have recently been published. Nishioka and Fujita<sup>36</sup> studied the early to intermediate phases of binary nucleation in the  $\text{H}_2\text{SO}_4\text{-H}_2\text{O}$  system, but due to computational limitations they were unable to follow this very slowly relaxing system all the way to steady state. Kožíšek and Demo<sup>37,38</sup> restricted their work to binary systems that form ideal mixtures in the nucleated phase. Here, we shall provide a much more detailed look at the full transient period for six binary systems representing a wide range of ideal and nonideal solution behavior. Our specific goals are to examine how the two-dimensional distributions of cluster concentrations and fluxes evolve to their steady state values and to stringently test the available expressions for the time lag in binary nucleation. To determine how robust these expressions are, we examine how the time lag depends on several binary system parameters including impingement rates, equilibrium vapor pressures, vapor phase activities, and the degree of liquid phase nonideality. We are particularly interested in understanding how the time lag for the saddle point flux varies under certain limiting or special conditions that occur, for example, when the concentration of one component approaches zero, or when ridge crossing is the dominant steady state pathway for particle formation. Although all of our calculations are for vapor-liquid phase transitions, the general conclusions we draw should apply equally well to condensed phase systems. In Sec. II of this paper we describe the kinetics equations we solved, how we derive the estimates for the time lag from the numerical data, and the available analytical expressions for  $t^*$  in binary systems. Our results are presented and discussed in Sec. III. We conclude with a very brief summary of the results in Sec. IV.

## II. COMPUTATIONAL METHODOLOGY

As discussed in more detail in WWII, we solved the kinetics equations describing binary nucleation<sup>39</sup> assuming that the growth and decay of clusters proceeds only by the

addition or loss of monomers. Under these conditions, the change with time of the number density  $f(i,j,t)$  of clusters of composition  $(i,j)$  is given by

$$\frac{df(i,j,t)}{dt} = J_A(i-1,j,t) - J_A(i,j,t) + J_B(i,j-1,t) - J_B(i,j,t), \quad (2)$$

where the fluxes between adjacent cluster sizes,  $J_A$  and  $J_B$ , are written as

$$J_A(i,j,t) = \Gamma_A(i,j)N_A f(i,j,t) - E_A(i+1,j)f(i+1,j,t), \quad (3)$$

and

$$J_B(i,j,t) = \Gamma_B(i,j)N_B f(i,j,t) - E_B(i,j+1)f(i,j+1,t). \quad (4)$$

Here,  $\Gamma_\nu(i,j)$  is the forward rate coefficient for adding a monomer of type  $\nu$  to a cluster containing  $i$  molecules of species  $A$  and  $j$  molecules of species  $B$ ,  $E_\nu(i,j)$  is the reverse rate coefficient for removing a monomer of species  $\nu$  from a cluster with composition  $(i,j)$ , and the monomer concentrations are defined as  $N_A = f(1,0,t)$  and  $N_B = f(0,1,t)$ . The forward rate coefficients are given by the kinetic theory expression for the collision frequency between two particles of unequal mass assuming a unit mass accommodation coefficient for each species. The reverse rate coefficients are obtained from the forward rate coefficients and the equilibrium cluster size distribution by using the principle of detailed balance. As noted previously,<sup>35,40</sup> for large  $i$  and  $j$  the rate coefficients asymptotically approach the expressions used in conventional binary nucleation theory. For small  $i$  and  $j$  the rate coefficients differ from the conventional ones because of the various self-consistency corrections that we introduced. Explicit expressions for the rate coefficients and the equilibrium distribution are available in the first two papers of this series.<sup>35,40</sup> The kinetics equations were solved subject to the following initial and inner boundary conditions:

$$f(i,j,0) = 0, \quad i+j > 1, \quad (5a)$$

$$f(1,0,t) = N_A, \quad t \geq 0, \quad (5b)$$

$$f(0,1,t) = N_B, \quad t \geq 0. \quad (5c)$$

The boundaries of the rectangular computational grid are set by the maximum values of  $i$  and  $j$ ,  $i_{\max}$  and  $j_{\max}$ , respectively. Rather than introducing a sink at the edge of the grid by setting  $f(i_{\max},j,t) = f(i,j_{\max},t) = 0$ , we estimate the concentrations of the largest clusters by logarithmically extrapolating the concentrations of smaller clusters at the previous time step. At  $i = i_{\max}$ , for example,  $f(i_{\max},j,t) = f(i_{\max}-1,j,t-1)^2 / f(i_{\max}-2,j,t-1)$ . This results in a smoother variation in the cluster concentration as the edge of the grid is approached, and the effect is to mimic a somewhat larger grid. Runs with different grid sizes gave invariant results as long as the grid was large enough. Our computations were performed on a Digital 3000/300 AXP workstation. For an  $80 \times 80$  grid, 6238 equations were solved in about 8 h of

CPU time for the “stiffest” conditions considered. For milder conditions, less CPU time was needed.

Our computational code normally stores the values of all cluster compositions  $f(i, j, t)$  and all fluxes between adjacent cluster sizes,  $J_A(i, j, t)$  and  $J_B(i, j, t)$ , at 20 times, logarithmically spaced in the integration interval. To provide better time resolution, 80 intermediate values are stored for a few cluster compositions in the saddle region. The code also stores the total flux crossing lines of constant  $i + j$  at 80 logarithmically spaced times. At steady state each of these sums equals the nucleation rate. Under transient conditions these sums are more difficult to interpret because they usually contain contributions from both subcritical and supercritical fluxes. As in unary nucleation,<sup>6</sup> the transient fluxes for subcritical cluster sizes overshoot their steady state values while supercritical fluxes take longer to reach their steady state values than does the critical flux.<sup>37</sup> To avoid this complication in our time lag calculations, we used the well-defined flux through the saddle point

$$J^*(t) = J_A(i^*, j^*, t) + J_B(i^*, j^*, t) \quad (6)$$

to compute numerical time lags.

By analogy with the definition for unary systems,<sup>4</sup> we define<sup>41</sup> the time lag for the saddle point flux,  $t^*$ , as

$$t^* = \int_0^\infty \left| 1 - \frac{J^*(t)}{J^*} \right| dt, \quad (7)$$

where  $J^*$  is the steady state value of  $J^*(t)$ , which is not identical to the total steady state nucleation rate. We use the fluxes stored at intermediate times to directly integrate Eq. (7) and call this the numerical time lag,  $t_{\text{num}}^*$ .

Many exact and approximate expressions have been developed for  $t^*$  in unary nucleation; see, for example, Refs. 3–5, 7, 9–11, 13–22, 26, and 30. Only two analytical expressions are available for binary nucleation.<sup>30,33</sup> The first is the estimate for the time lag at the saddle point developed by Wilemski,<sup>30</sup>

$$t_W^* = \tau_W L(w^*, n^*) = \frac{3n^*}{D_{\text{av}}^* \ln S^*} L(w^*, n^*), \quad (8a)$$

where  $\tau_W$  is a characteristic time scale for binary nucleation determined by the collision frequency of the monomers with a critical cluster containing  $n^*$  monomers,  $n^* = i^* + j^*$ . The average impingement rate,  $D_{\text{av}}^*$ , is given by

$$D_{\text{av}}^* = \frac{\Gamma_A^* \Gamma_B^* N_A N_B}{\Gamma_A^* N_A x_B^2 + \Gamma_B^* N_B x_A^2}, \quad (8b)$$

where  $\Gamma_\nu^* = \Gamma_\nu(i^*, j^*)$ . The effective critical supersaturation  $S^*$  is given by

$$\ln S^* = x_A \ln S_A + x_B \ln S_B, \quad (8c)$$

where  $S_\nu = N_\nu / N_\nu^\infty(x_\nu)$  and  $N_\nu^\infty(x_\nu)$  is the number concentration of vapor molecules of type  $\nu$  in equilibrium with a bulk solution of composition  $x_\nu$  (e.g.,  $x_B = j^*/n^*$ ). The function  $L$  depends primarily on the dimensionless barrier height  $w^* = W^*/kT$ , where  $W^*$  is the reversible work required to form a cluster of composition  $(i^*, j^*)$  from the gas phase.

For our calculations we assumed ideal gas behavior and the capillarity approximation for  $W(i, j)$ . Wilemski originally evaluated  $L(w^*, n^*)$  numerically. His formal expression, however, is functionally identical for binary and unary nucleation and is equivalent to more recent unary time lag expressions.<sup>19,20</sup> This equivalence provides a more convenient way to evaluate  $L$  for binary systems using the asymptotic results derived for unary time lags. With the usual parabolic approximation for  $W^*$ , Shneidman and Weinberg<sup>20</sup> found

$$L(w^*) = \frac{1}{2} \left( \ln \frac{w^*}{3} + \gamma_E \right), \quad (8d)$$

where  $\gamma_E = 0.5772 \dots$  is the Euler–Mascheroni constant. Wu’s result<sup>19</sup> is similar but less precise. We will demonstrate later that Eq. (8d) gives results that are very similar to a simple parametrization for  $L(w^*, n^*)$  using the numerical values presented in Table III of Wilemski’s original paper. Adding the small nonparabolic correction term of Shneidman and Weinberg<sup>20</sup> to Eq. (8d) gives even better agreement. As discussed below, however, the parabolic approximation provides a more appropriate basis for comparing the different theoretical results.

The second expression, derived by Shi and Seinfeld,<sup>33</sup> is given by

$$t_{\text{SS}}^* = \frac{\tau_{\text{SS}}}{2} [E_1(e^{2\lambda_{\text{SS}}}) + \gamma_E + 2\lambda_{\text{SS}}]. \quad (9)$$

Here,  $E_1$  is the exponential integral, and  $\tau_{\text{SS}}$  is a characteristic time scale for binary nucleation given by

$$\tau_{\text{SS}} = (2u)^{-1}, \quad (10)$$

where  $u$  is defined as

$$u = -[D_{AA} + D_{BB} - ((D_{AA} - D_{BB})^2 + 4D_{AB}^2)^{1/2}]/2, \quad (11)$$

and

$$D_{\alpha\beta} = (\Gamma_\alpha^* \Gamma_\beta^* N_\alpha N_\beta)^{1/2} w_{\alpha\beta}^*. \quad (12)$$

The second derivatives of  $w(i, j)$  with respect to  $i$  and  $j$  at the saddle point are denoted by  $w_{\alpha\beta}^*$ .

For gas-phase nucleation, the expression for  $\lambda_{\text{SS}}$  derived by Shi and Seinfeld is

$$\lambda_{\text{SS}} = \sqrt{3} \left( \frac{\pi}{3} - \tan^{-1} \frac{1 + 2\xi_0}{\sqrt{3}} \right) + \ln \left[ \frac{3(1 - \xi_0)\sqrt{3u}}{c\sqrt{1 + \xi_0 + \xi_0^2}} \right], \quad (13)$$

where  $\xi_0$  is the value of

$$\xi = (1 + cx)^{1/3} \quad (14)$$

evaluated at  $i = 1$  and  $j = 1$ . The value of  $c$  is given by

$$c = \frac{(\Gamma_A^* N_A)^{1/2} \cos \alpha + \mu (\Gamma_B^* N_B)^{1/2} \sin \alpha}{i^* + \mu j^*}, \quad (15)$$

where  $\mu$  is the ratio of  $A$  and  $B$  monomer volumes and the angle  $\alpha$  is given by<sup>42</sup>

$$\tan \alpha = \frac{1}{2D_{AB}} [D_{BB} - D_{AA} - ((D_{AA} - D_{BB})^2 + 4D_{AB}^2)^{1/2}]. \quad (16)$$

Finally, the rotated coordinate  $x$  is given by

$$x = X \cos \alpha + Y \sin \alpha, \quad (17)$$

where, in our notation,  $X = (i - i^*)/(\Gamma_A^* N_A)^{1/2}$  and  $Y = (j - j^*)/(\Gamma_B^* N_B)^{1/2}$ .

By comparing Eqs. (8a) and (9) and recognizing that  $E_1(e^{2\lambda}) \ll 1$  for all relevant values of  $\lambda$ , we see that  $L(w^*, n^*)$  corresponds to  $\lambda_{SS} + \gamma_E/2$  in the Shi–Seinfeld result. Although  $L(w^*, n^*)$  actually contains information about the nonparabolic form of  $W$ , a more appropriate comparison between the theories of Wilemski and Shi and Seinfeld is one based on Eq. (8d) for  $L$  because Shi and Seinfeld worked solely in the parabolic approximation. Restricting ourselves to the parabolic approximation, we see that the term  $\ln(w^*/3)$  corresponds to  $2\lambda_{SS}$ , and thus each theory can be characterized by two parameters  $\tau$  and  $\lambda$ ,

$$t^* = \tau(\lambda + \gamma_E/2). \quad (18)$$

For degenerate binary systems, the characteristic time scales  $\tau_W$  and  $\tau_{SS}$  are identical, and for the conditions and systems explored in this work, they are also generally of comparable value. As we shall see, the major quantitative differences between the two theories stems from the parameter  $\lambda$ .

In addition to calculating  $t^*$ , we use the appropriate values for  $\tau$  and  $\lambda$  to directly compare the time dependent behavior of the numerical saddle point flux  $J^*(t)$  to the expected double exponential behavior<sup>13,15,17,22,33</sup> given by

$$J^*(t)/J^* = \exp(-\exp(2(\lambda - t/\tau))). \quad (19)$$

This type of time dependence was first found for supercritical particle fluxes,<sup>11</sup> although in this case the factor of 2 is absent in the inner exponential.

In our calculations we considered two ideal systems (*o*-xylene–*m*-xylene and ethanol–hexanol), two systems that exhibit negative deviations from ideality (dichloromethane–tetrahydrofuran and chloroform–tetrahydrofuran), and two model systems that exhibit positive deviations from ideality (PD1 and PD2). The two positively deviating pairs had the same physical properties as *o*-xylene–*m*-xylene (PD1) and ethanol–hexanol (PD2) but had excess Gibbs free energies of mixing given by  $g^E = Ax_Ax_B$ . Choosing the value of  $A$  so that  $A/RT = 2$  at the simulation temperature  $T$  put each positively deviating system at its upper critical solution temperature (UCST). Under these conditions the free energy surface still has a single well-defined analytical saddle point but the saddle region is extremely broad. The physical properties used as input for the calculations are documented in Appendix B of WWII.<sup>43</sup>

### III. RESULTS AND DISCUSSION

#### A. Evolution of cluster concentrations and fluxes

Solving the full set of kinetics equations in time rather than simply finding the steady state solution gives valuable

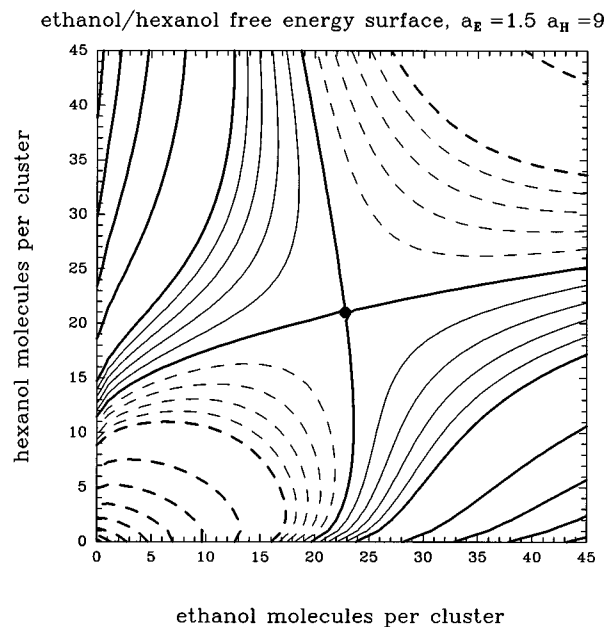


FIG. 1. Contour plot of the free energy surface for the ethanol–hexanol system at vapor activities of  $a_E = 1.5$  and  $a_H = 9$ . The analytical saddle point  $\bullet$  is located at the junction of the intersecting contours, where  $(i^*, j^*) = (22.5, 20.8)$  and  $w^* = 42.4$ . The solid contour lines denote free energies above the saddle point value, and the dashed contours denote free energies below the saddle point. The heavy contour lines are spaced at  $5kT$  intervals, and the light contours are spaced at  $1kT$  intervals relative to the saddle point free energy.

insight into the dynamics of the transient state and permits us to calculate directly any time lag of interest. The other quantities of interest are the transient fluxes,  $J(i, j, t) = J_A(i, j, t) + J_B(i, j, t)$ , the cluster concentrations,  $f(i, j, t)$ , and the ratios of nonequilibrium to equilibrium cluster concentrations,  $f(i, j, t)/N(i, j) (\equiv \Phi(i, j, t))$ . Although we examined systems with a wide range of liquid phase nonideality, our general discussion of transient behavior will focus on binary nucleation in the ideal ethanol–hexanol system. This system is interesting because of the large disparity in the equilibrium vapor pressures of the pure components. For example, at our simulation temperature, 260 K, the ratio of equilibrium monomer number densities  $N_E^\infty/N_H^\infty$  is 226. This disparity gives rise to a large difference in the monomer impingement rates and, hence, in the forward reaction rates<sup>44</sup> while the saddle point is still far from either pure component axis. At steady state, significant differences can therefore exist between the Reiss<sup>39</sup> and Stauffer<sup>45</sup> formulations for the nucleation rate.<sup>35</sup> Moreover, the transient calculations are affected by this disparity in the forward reaction rates because the times required for the pure cluster concentrations to approach their steady state values differ by more than an order of magnitude. Although this difference in time scales is significant, it does not stop our differential equation solver from evolving the rate equations into the steady state. In contrast, for the extreme case of  $H_2SO_4$ – $H_2O$  examined by Nishioka and Fujita,<sup>36</sup> the much larger time scale differences did preclude the attainment of steady state. An examination of transient behavior for ethanol–hexanol is also of interest because

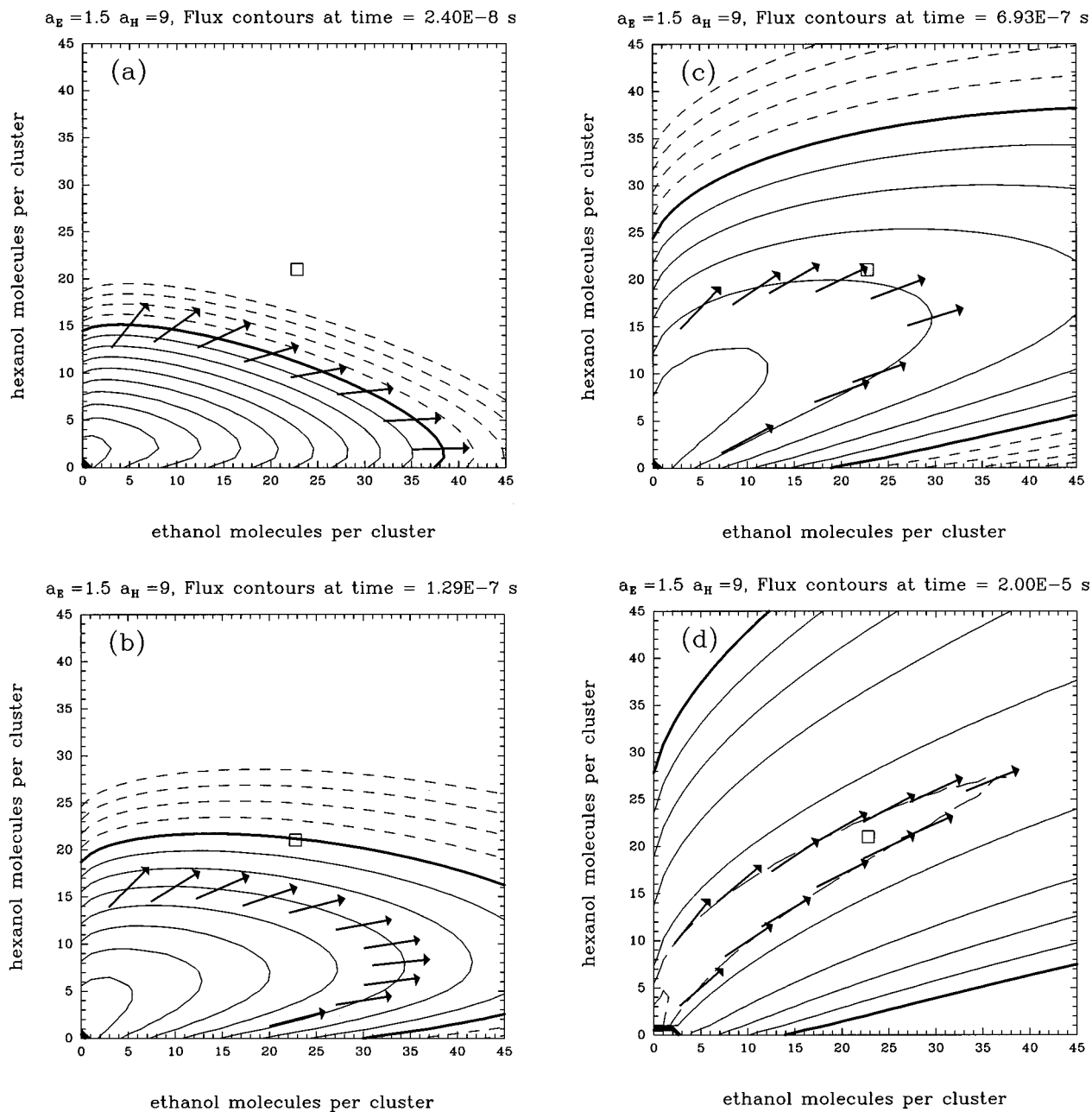


FIG. 2. Contours of constant flux,  $J(i, j, t) = J_A(i, j, t) + J_B(i, j, t)$ , for the ethanol-hexanol system at four times for vapor activities  $a_E = 1.5$  and  $a_H = 9$ . The heavy contour lines correspond to a flux of  $1 \text{ cm}^{-3} \text{ s}^{-1}$ . The light solid lines correspond to fluxes greater than  $1 \text{ cm}^{-3} \text{ s}^{-1}$  and the short dashed lines correspond to fluxes less than  $1 \text{ cm}^{-3} \text{ s}^{-1}$ . The contour spacing is two orders of magnitude in flux. The arrows indicate the local direction of the flux along one of the contours. The saddle point is marked by the open square. (a) The contours of constant flux extend further along pure ethanol axis than along the hexanol axis. (b) The region with the highest flux begins to swing away from the ethanol axis toward the saddle point as the fluxes along the ethanol axis decrease. (c) The region with the highest flux continues to move towards the saddle point, and the fluxes in the ethanol-rich region decrease rapidly. (d) At steady state, the highest flux flows through the saddle region along a path that depends on the shape of the free energy surface and on the relative monomer impingement rates. The long dashed lines represent contours at  $\log_{10}(J(i, j, t)) = 8.5$  and  $9$ . This figure is equivalent to the steady state flux plot presented in Fig. 2(b) of Ref. 35.

nucleation rates have been measured for this system in an expansion cloud chamber at 260 K.<sup>46</sup> Thus these calculations will confirm that the expansion rates used in these experiments were small enough to ensure that steady state nucleation was obtained.

Figure 1 illustrates a typical free energy surface for the ethanol-hexanol system. At the conditions indicated in the

figure,  $N_E/N_H = 37$ , and the ratio of ethanol and hexanol monomer impingement rates is 56. Figures 2 and 3 show how the values of  $J(i, j, t)$  and  $\Phi(i, j, t)$ , respectively, evolve to the steady state at these conditions. The first three times in each figure represent transient states, whereas the final time is about an order of magnitude larger than  $t^*$ . The grid size

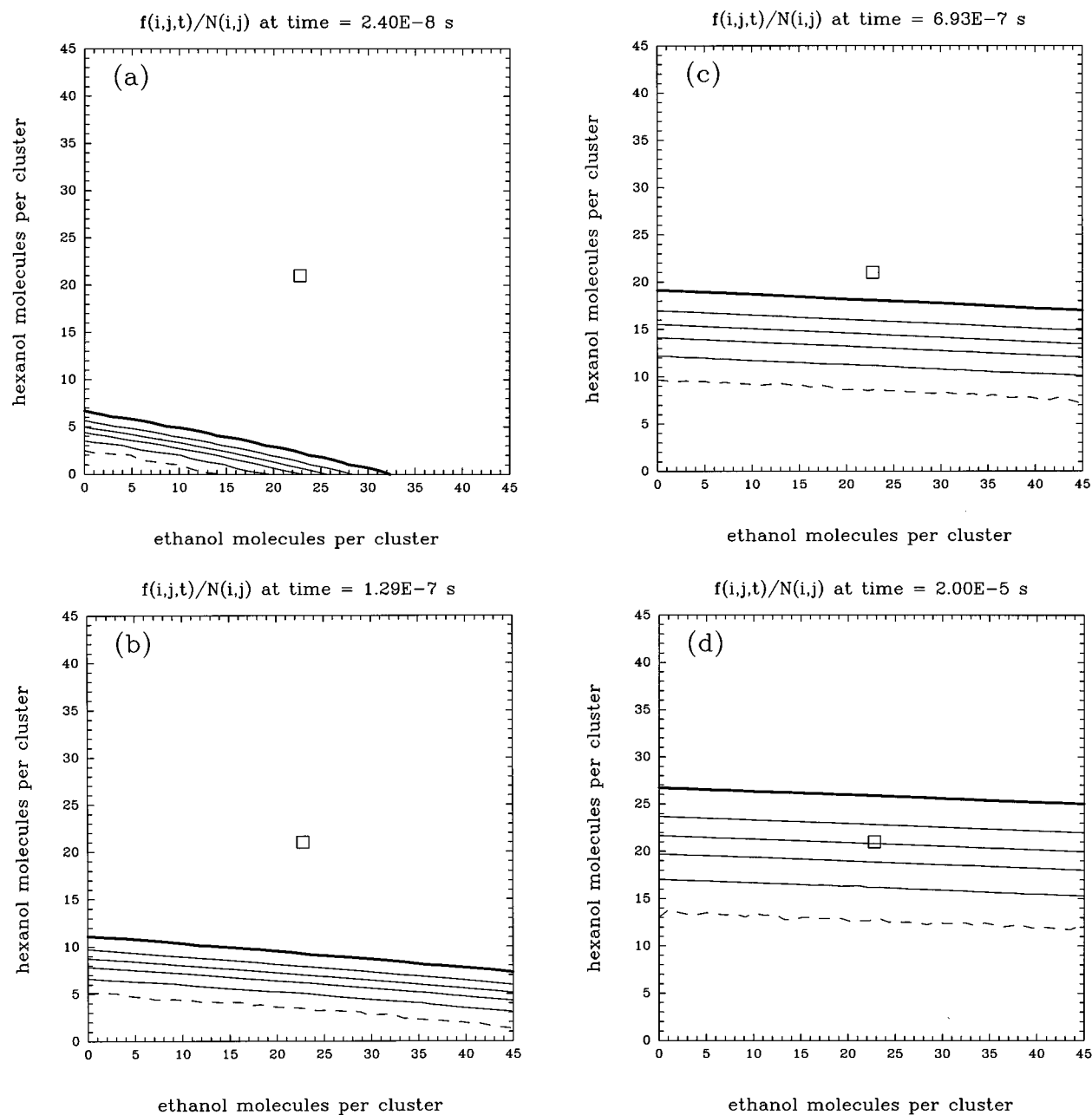


FIG. 3. Contours of constant  $\Phi(i,j,t)$  at three transient times and at steady state for vapor activities  $a_E=1.5$  and  $a_H=9$ . The heavy contour line corresponds to  $\Phi(i,j,t)=0.1$ . The light solid lines correspond to higher values of  $\Phi(i,j,t)$  and increase in steps of 0.2. The short dashed line corresponds to  $\Phi(i,j,t)=0.99$ . The saddle point is marked by the open square. (a) Ethanol-rich clusters approach their equilibrium concentrations more rapidly than do hexanol-rich clusters. (b) and (c) The contours spread out and become more horizontal as they approach the saddle point. (d) At steady state, the contours are almost parallel to the ethanol axis. At the saddle point  $\Phi(i,j,t)=0.5$ .

used in these simulations was  $80 \times 80$ , but for clarity we restricted the figures to a grid size of  $45 \times 45$ .

As illustrated in Fig. 2(a), at the earliest times the higher impingement rate of ethanol dictates that the particle fluxes build up more rapidly in the direction of the ethanol axis. At these early times, the net fluxes between adjacent cluster sizes are essentially equal to the forward fluxes. At somewhat later times, in Figs. 2(b) and 2(c), the fluxes near the pure ethanol axis decrease, and the region of highest flux swings toward the saddle. The flux decrease occurs because

the early surge in ethanol-rich cluster production is damped as the rates of the various cluster decay steps gradually increase. At the same time, with progress curtailed in the ethanol-rich direction, the slower kinetics of hexanol addition gradually influences the overall course of cluster formation. In Fig. 2(c), the region of highest flux is still located primarily below the saddle point, and it extends considerably up the ridge that lies between the saddle point and the pure ethanol axis. The particle formation process now resembles steady state ridge crossing nucleation, cf. Fig. 5(b) in WWII,

although here this state is an intermediate stage en route to saddle point nucleation. Finally, in Fig. 2(d) we see the relatively narrow steady state nucleation path whose course is influenced both by the shape of the underlying free energy surface and the kinetics of monomer addition.

Although not illustrated, the buildup of the cluster concentrations occurs in a qualitatively similar manner. The concentration of ethanol-rich clusters increases more rapidly than the concentration of hexanol-rich clusters. This buildup of ethanol-rich clusters is similar to the initial rapid formation of water-rich clusters observed by Nishioka and Fujita<sup>36</sup> in their simulations of transient binary nucleation in the  $\text{H}_2\text{SO}_4\text{-H}_2\text{O}$  system. At steady state, there is a broad region of elevated cluster concentrations extending from the monomers through the saddle to the stable particles of the new phase.

A much simpler picture emerges when we examine the transient behavior of  $\Phi(i, j, t)$ . As illustrated in Fig. 3, in this ideal system the contours form a set of straight, parallel lines. Ethanol-rich clusters reach their steady state concentrations much more quickly than do the hexanol-rich clusters. As the region of the grid with  $\Phi \geq 0.99$  expands to contain clusters with progressively more hexanol molecules, the difference in time scales for ethanol and hexanol leads to contours that are almost parallel to the ethanol axis and to the large increase in the region of quasiequilibrium along the ethanol axis.  $\text{H}_2\text{SO}_4\text{-H}_2\text{O}$  is the classic example of a system in which the quasiequilibrium region is not confined to its usual location near the origin but forms a strip extending along the axis of the component (water) with the shorter time scale.<sup>47,48</sup> As in unary nucleation, Fig. 3(d) shows that the critical cluster concentration equals one half of the equilibrium value at steady state.

The qualitative behavior shown in Fig. 3 does not seem to depend on the specific values used for the gas species activities and, hence, for the impingement rates. We have found that it occurs even, for example, when the hexanol impingement rate greatly exceeds that of ethanol and unary nucleation of hexanol is the dominant kinetic process. The spacing and absolute locations of the contour lines are, however, affected by the activity values. This tendency to rapidly “equilibrate” with respect to ethanol, regardless of the actual gas species impingement rates, is connected to the tendency of the evaporation rate of ethanol ( $A$ ) to exceed that of hexanol ( $B$ ) for most cluster compositions. Aside from Kelvin and compositional factors, each  $E_\nu$  is determined primarily by the equilibrium monomer number density of pure species  $\nu$ .<sup>40</sup> Thus the large inequality of the equilibrium vapor pressures in this system results in the corresponding disparity,  $E_A \gg E_B$ , for almost all cluster compositions. The compositional variation of  $E_A$  and  $E_B$  reduces the inequality for small values of  $n_A$  (and can reverse it for large values of  $n_B$ ), but in the subcritical region this effect is small.

Some additional appreciation for this behavior can be gained by transforming Eq. (2) into an equation for the time evolution of  $\Phi$ . Similar transformations have previously been used in studies of binary nucleation kinetics.<sup>33,37,38,48</sup> To do this, we use detailed balance relations<sup>40</sup> to replace the

forward rate coefficients,  $\Gamma_A$  and  $\Gamma_B$ , by the corresponding evaporation rate coefficients,  $E_A$  and  $E_B$ , and we change to continuous composition variables ( $i \rightarrow n_A$ , and  $j \rightarrow n_B$ ) to keep the final form more compact. The result is a complementary version of the equation that forms the basis for the analytical analysis of transient behavior in unary<sup>11,15</sup> and binary<sup>33</sup> systems,

$$\frac{\partial \Phi(n_A, n_B, t)}{\partial t} = \sum_{\nu=A,B} \left[ \frac{\partial}{\partial n_\nu} \left( E_\nu \frac{\partial \Phi}{\partial n_\nu} \right) + E_\nu \left( \frac{\partial \ln N}{\partial n_\nu} \right) \frac{\partial \Phi}{\partial n_\nu} \right]. \quad (20)$$

The important difference between these earlier equations and ours is that in Eq. (20) the “diffusion coefficients” are equal to  $E_A$  and  $E_B$ , rather than  $\Gamma_A N_A$  and  $\Gamma_B N_B$ . This form is advantageous because it shows how the disparity between  $E_A$  and  $E_B$  is responsible for the rapid increase of  $\Phi$  in the  $A$  direction and for its much slower progress in the  $B$  direction. Moreover, in the usual ideal gas approximation,  $E_A$  and  $E_B$  are independent of the gas phase activities and the total pressure. This explains why the qualitative behavior of  $\Phi$  has a “universal” character to it: Changes in the vapor phase activities will only weakly affect the time evolution of  $\Phi$  through the components of the “drift” velocity,  $E_\nu (\partial \ln N / \partial n_\nu)$ . These velocity components depend logarithmically on the activities, and they vanish at the saddle point. Consequently, the transient and steady state contour plots of  $\Phi$  for each system have a characteristic “signature” that depends predominantly on the relative sizes of  $E_A$  and  $E_B$ . We will discuss this more extensively in a later paper.

Although not illustrated here, the time evolution of the fluxes in the PD2 system mirrors the transient behavior illustrated in Fig. 2 quite closely. When ridge crossing nucleation is the steady state solution, the location of the saddle point is in the vicinity of the pseudo-hexanol ( $B$ ) axis. The impingement rate of pseudoethanol ( $A$ ), however, is still significantly higher than that of  $B$ . Because of this disparity in impingement rates, the region of highest flux initially hugs the  $A$  axis and then moves away from it towards the saddle point. However, unlike the ethanol-hexanol case, the region with the highest particle flux gets “stuck” and never reaches the saddle point. Rather, as illustrated in Fig. 4(b) of WWII, at steady state it avoids the saddle point and passes over a low ridge in the free energy surface. In a sense, ridge crossing nucleation arises naturally out of what is normally an intermediate state in the development of saddle point nucleation.

For systems whose pure components have comparable equilibrium vapor pressures, for example  $o$ -xylene- $m$ -xylene, the initial cluster buildup is still driven in the direction of the species with the higher impingement rate. The region with the highest cluster concentrations and the highest fluxes still swings from near the axis of the dominant species to the saddle point. The difference is that for systems with comparable equilibrium vapor pressures, a large difference in the impingement rates occurs only when there is a correspondingly large difference in the vapor phase activities. For these systems, the difference in vapor phase activities forces

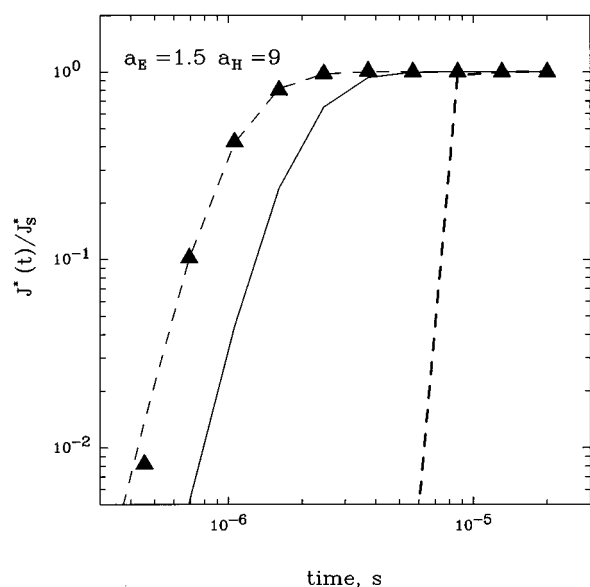


FIG. 4. Numerical values (solid triangles) of the transient nucleation rates at the saddle point are compared with the analytical predictions of Eq. (19) for ethanol–hexanol vapor activities as indicated. The solid line uses  $\tau = \tau_W$  and the parabolic approximation  $\lambda = \lambda_p$  where  $2\lambda_p = \ln(w^*/3)$ , the heavy dashed line uses  $\tau = \tau_{SS}$  and  $\lambda = \lambda_{SS}$ , where  $\lambda_{SS}$  is given by Eq. (13), and the light dashed line uses  $\lambda = \lambda_p$  and  $\tau = \tau_{adj}$ , where  $\tau_{adj}$  is a value adjusted to better fit the numerical results.  $\tau_W = 1.403 \mu\text{s}$ ,  $\lambda_p = 1.325$ ,  $\tau_{SS} = 1.204 \mu\text{s}$ ,  $\lambda_{SS} = 5.617$ , and  $\tau_{adj} = 0.760 \mu\text{s}$ .

the saddle point to be located near the axis of the dominant species and the region of highest flux always lies reasonably close to the line joining the “origin” to the critical cluster composition.

## B. Time lags and the transient saddle point flux

Calculating time lags requires much less effort than and is often as useful as solving the full set of kinetics equations. As discussed earlier, the two time lag expressions presented in Sec. II both depend on the parameters  $\tau$  and  $\lambda$ . The characteristic time,  $\tau$ , is related to the rate of monomer impingement for the critical cluster size, and  $\lambda$  is a parameter that characterizes the free energy barrier. As seen in Eq. (19), these parameters also control the transient behavior of the saddle point flux. For *o*-xylene–*m*-xylene, which is essentially a degenerate binary mixture, the two characteristic times,  $\tau_W$  and  $\tau_{SS}$ , are practically identical. Even for the many nonideal systems we examined, the two characteristic times rarely differed by more than 1%–10% with  $\tau_W$  always greater than  $\tau_{SS}$ . In the worst cases, we found  $\tau_W/\tau_{SS} \approx 2$ –3. These extreme differences occurred in two instances: (1) in the ethanol–hexanol system for the transition to unary nucleation of ethanol and (2) in the PD2 system in and near regions of ridge crossing. The differences are the result of a discrepancy between the angles  $\theta$  and  $\alpha$  implicit in the two expressions for  $\tau$ .

Before discussing our results for the time lags, we first show a representative comparison, in Fig. 4, of our numerical transient results for the saddle point flux with the analyti-

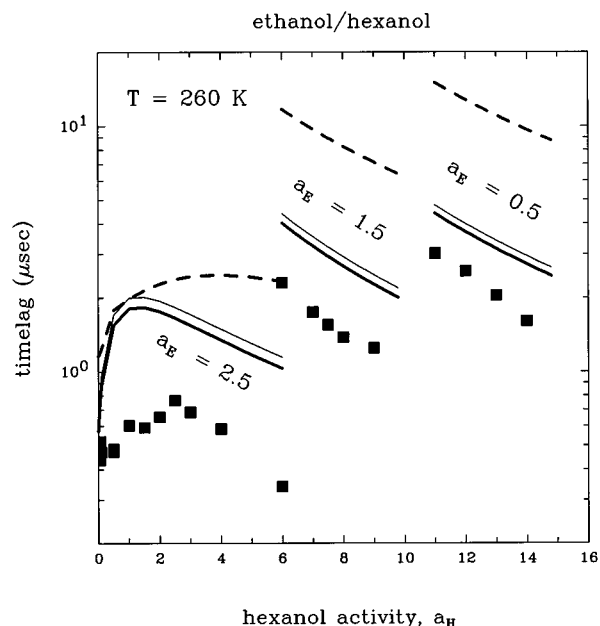


FIG. 5. Several analytical estimates for  $t^*$  are compared with the values of  $t_{num}^*$  (solid squares) for ethanol–hexanol at the indicated ethanol activities. The light solid line corresponds to  $t^*$  calculated using  $\tau_W$  and a parametrized fit to the values given in Table III of Ref. 30,  $L(w^*, n^*) = -0.76 + 1.40[w^*(1 + 2/n^* - 3(n^*)^{-2/3})]^{1/6}$ . The heavy solid line uses  $\tau_W$  and Eq. (8d). The heavy dashed lines correspond to  $t_{SS}^*$ .

cal results given by Eq. (19). The comparison is made for the same conditions used in Figs. 1–3. The solid line corresponds to using  $\tau_W$  and  $2\lambda = \ln(w^*/3)$ , and the heavy dashed line uses  $\tau_{SS}$  and  $\lambda_{SS}$ . Neither curve agrees quantitatively with the numerical results although the slope of the solid line looks reasonable. Since the slope of  $\ln J$  is dominated by  $\lambda$  and since  $J^*(t)/J^* \approx 0.95$  when  $t = (\lambda + 3/2)\tau$ , modest changes in  $\tau$  at constant  $\lambda$  will shift the curves along the time axis without greatly affecting the slope. The light dashed line uses  $2\lambda = \ln(w^*/3)$  with the value of  $\tau$  adjusted to better fit the numerical results. In general we find that the double exponential form of Eq. (19) fits our numerical results well in the range  $0.01 \leq J^*(t)/J^* \leq 1$ , that  $(1/2)\ln(w^*/3)$  is a better estimate for  $\lambda$  than Eq. (13), and that both  $\tau_W$  and  $\tau_{SS}$  overestimate the value of  $\tau$ .

An independent test for the consistency of our numerical data with the double exponential form relies on the following special property:<sup>49</sup>

$$J^*(t^*)/J^* = \exp(-\exp(-\gamma_E)) = 0.57. \quad (21)$$

This result, which also holds for supercritical particle fluxes,<sup>50</sup> follows directly from Eqs. (18) and (19) and does not depend on the values of  $\tau$  or  $\lambda$ . The value of  $t^*$  for which our numerical data in Fig. 4 satisfy Eq. (21) agrees well with the value found by numerically integrating Eq. (7). Equation (21) thus provides an alternative means of estimating the numerical time lag that avoids the time integral in Eq. (7). We found similar consistency in the other cases we examined.

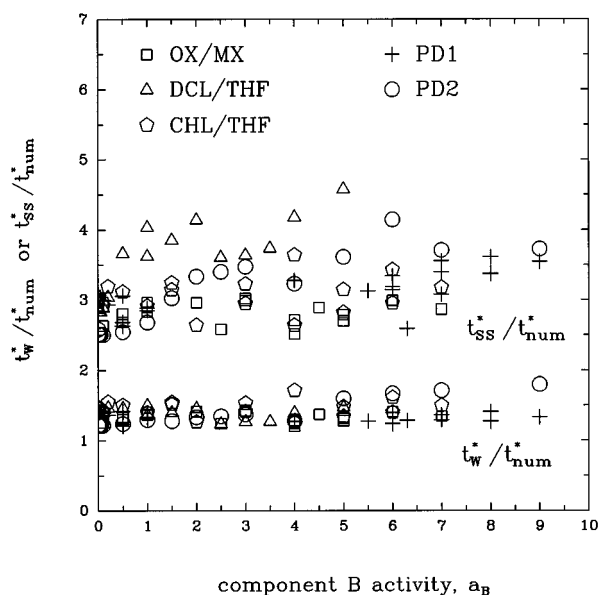


FIG. 6. The values of  $t_w^*/t_{num}^*$  and  $t_{SS}^*/t_{num}^*$  are quite constant over a wide range of gas phase activities indicating that the analytical theories predict the relative time lag behavior quite well. The values of  $t_w^*$  are calculated using Eq. (8d). The five binary systems considered here include *o*-xylene-*m*-xylene (OX/MX), dichloromethane-tetrahydrofuran (DCM/THF), chloroform-tetrahydrofuran (CHL/THF), the model positively deviating system PD1, and the model positively deviating system PD2.

We now present our time lag results beginning with the ethanol-hexanol system. In Fig. 5 we compare several analytical predictions for the time lag with our numerical results calculated by integrating Eq. (7). The solid lines were calculated using Eq. (8a) and either a parametrized fit to the values of  $L(w^*, n^*)$  given in Table III of Wilemski's original paper<sup>30</sup> or Eq. (8d). These two estimates agree quite well over the entire range of activities. Although not shown here, adding the constant nonparabolic correction ( $=\ln 3 - 1$ ) of Shneidman and Weinberg<sup>20</sup> to Eq. (8d) makes these two curves practically coincide, although, curiously, it further diminishes the agreement with the numerical results. The Shi-Seinfeld estimates,<sup>33</sup> given by the heavy dashed lines, are roughly three times higher than the other estimates just discussed. We note that since  $\tau_w$  and  $\tau_{SS}$  are essentially equal over most of this range of activity, the differences are due to values of  $\lambda_{SS}$  that are too large. This is a consequence of using the parabolic approximation for  $W$  to treat the time evolution of subcritical clusters. Shi and Seinfeld have themselves noted that their use of this approximation would overestimate the value of  $\lambda$ .<sup>51</sup>

As summarized in Fig. 6 for the other five systems, the ratios  $t_w^*/t_{num}^*$  and  $t_{SS}^*/t_{num}^*$  are remarkably consistent over a wide range of vapor phase activities. The quantitative agreement between  $t_w^*$  and  $t_{num}^*$  found here is actually better than for the ethanol-hexanol system, with  $t_w^*$  usually only overpredicting  $t_{num}^*$  by 25%–50%. The values of  $t_{SS}^*$  are again higher and do not approach the correct unary limit. As for ethanol-hexanol, this is due to overly large values of  $\lambda_{SS}$  resulting from the quadratic approximation for  $W$ .<sup>51</sup>

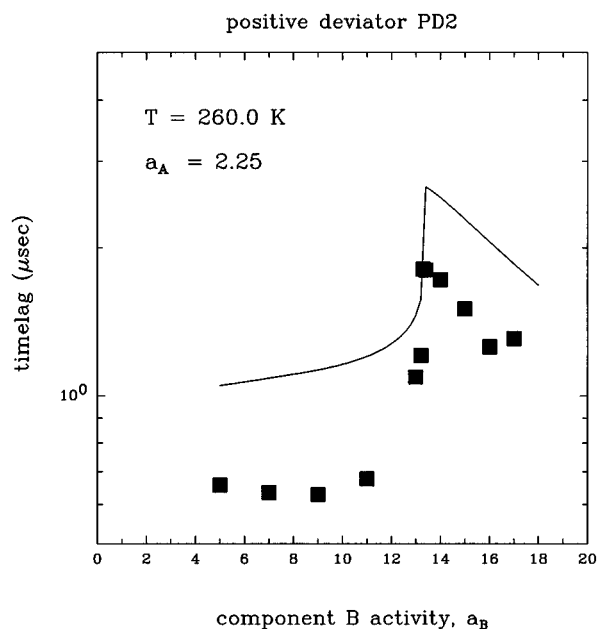


FIG. 7. The values of  $t_{num}^*$  (solid squares) are compared with  $t_w^*$  (solid line) for the model positively deviating system PD2, pseudoethanol(A)-pseudohexanol(B), in the region of ridge crossing. The values of  $t_w^*$  are calculated using Eq. (8d).

Despite the lack of quantitative agreement, the predicted analytical trends closely follow the numerical results. With the activity of one component fixed, increasing the activity of the second component almost always decreases the time lag. There are two reasons for this. First, an increase in the vapor phase activity increases the vapor phase concentration and thus the impingement rate of the monomers. This usually decreases  $\tau$ . In addition, a higher vapor phase activity decreases the height of the free energy barrier reducing the value of  $\lambda$ . There are, however, some notable exceptions (both real and apparent) to the rule that an increase in the gas phase activities and an increase in the nucleation rate are always accompanied by a decrease in the time lag. These include some transitions from unary to binary nucleation, as for ethanol-hexanol in Fig. 5, and situations in which ridge crossing nucleation dominates, as for the PD2 system in Fig. 7.

We will first discuss the ridge crossing case. In the region where steady state ridge crossing nucleation occurs, illustrated in Fig. 7 for the PD2 system at  $a_A = 2.25$ , the abrupt increase in time lag predicted by the analytical theory and observed in the numerical results is not the behavior that would be observed experimentally for the time lag of the system, although it signals that ridge crossing may be occurring. The problem is that in Fig. 7 we are plotting the analytical time lag for the flux through the *saddle point*. Our numerically derived time lags agree quite well with the analytical predictions because they are also calculated for the discrete saddle point. The sharp increase in the analytical time lag occurs because a slight increase in the activity of pseudoethanol forces the saddle point to move very rapidly

from a location near the pseudoethanol axis to one near the pseudo-hexanol axis. In a manner analogous to the ethanol–hexanol system illustrated in Fig. 3, the nucleation of clusters containing more pseudo–hexanol takes much longer to reach steady state. Although this behavior is correct for the saddle point flux, an observer counting the total number of particles produced [cf. Eq. (1)] should obtain a smaller and more smoothly varying value of  $t_g$ . As discussed earlier, ridge crossing nucleation is, in a sense, an intermediate state on the way to saddle point nucleation, and it is reasonable to expect that it should have a shorter development time.

Before discussing the other “anomalous” case, which involves the transitional behavior of the ethanol–hexanol system, it is instructive to examine the more usual time lag behavior in the transition region from binary to unary nucleation. For *o*-xylene–*m*-xylene, Fig. 8(a) shows that the time lag increases steadily as the activity of *m*-xylene is reduced, and it converges quite smoothly to the time lag for unary nucleation of *o*-xylene. This behavior is also observed for the dichloromethane–tetrahydrofuran, chloroform–tetrahydrofuran and PD1 systems. In all of these systems, the equilibrium vapor pressures and other physical properties of the pure components are quite similar, as are the evaporative time scales governing the evolution of  $\Phi$ . For ethanol–hexanol, illustrated more clearly in Fig. 8(b), the analytical time lag overshoots the unary value by a factor of 3 as the level of hexanol is reduced and only reaches the unary value when  $a_H < 0.01$ . Under these conditions, the analytical saddle point contains less than 0.25 hexanol molecules. Clearly, by this point unary nucleation is the dominant pathway. We emphasize that the numerical and analytical saddle point nucleation rates always agree to better than 10%. Based on close examination of the flux behavior in the region where binary nucleation is still important, ridge crossing is not occurring during this transition. Furthermore, there is no abrupt shift in the saddle point location. Nevertheless, the behavior shown in Fig. 8(b) is fundamentally the same as that observed in Fig. 7, but the increase in time lag in Fig. 8(b) should be experimentally observable unlike that in Fig. 7.

The “bump” in Fig. 8(b) directly reflects the difference in time scales for ethanol and hexanol impingement. In the transition from unary to binary nucleation, the critical cluster composition must become richer in hexanol. But, as illustrated in Fig. 3, the time required for hexanol-rich clusters to approach their steady state concentrations is longer than that for ethanol-rich clusters. At constant ethanol activity, the critical cluster becomes more hexanol-rich by both adding hexanol molecules and reducing the number of ethanol molecules. The maximum in the numerical time lags corresponds directly to those critical clusters with the highest absolute number of hexanol molecules. As  $a_H$  increases further, the number of hexanol molecules in the critical cluster actually decreases even though the hexanol mole fraction continues to rise. This is possible because the critical cluster size itself is shrinking. The decrease in the number of hexanol molecules in the critical cluster gives rise to a rapid decrease in the time lag. We noted earlier that the transient behavior of ethanol–hexanol is similar to that of  $\text{H}_2\text{SO}_4$ – $\text{H}_2\text{O}$ . Because

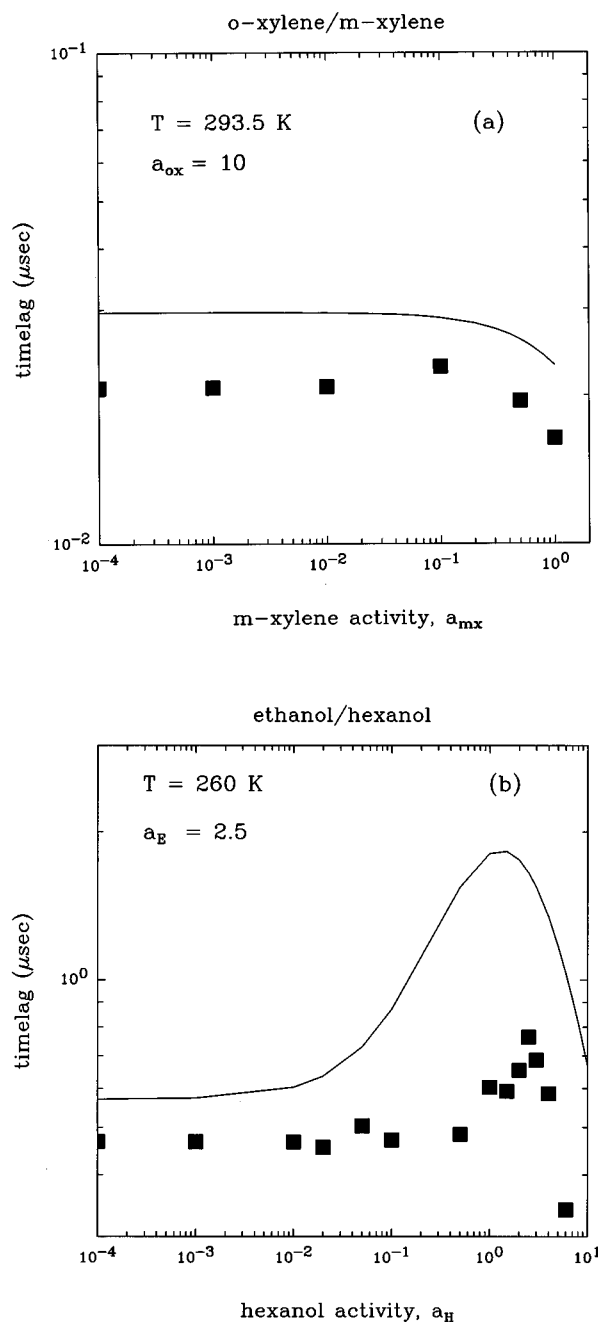


FIG. 8. The values of  $t_{num}^*$  (solid squares) are compared with  $t_W^*$  (solid lines) for the transition from binary to unary nucleation in two systems. The values of  $t_W^*$  are calculated using Eq. (8d). (a) For *o*-xylene–*m*-xylene, the binary time lag converges quite smoothly to the value for the unary time lag. (b) For ethanol–hexanol, the time lag exhibits a sharp maximum. For the numerical results, this maximum corresponds to the critical cluster composition with the highest absolute number of hexanol molecules.

the water and sulfuric acid time scales are so different, we expect to observe a much more pronounced increase in time lag in the transition from unary to binary nucleation for this system, except possibly when ridge crossing occurs.

#### IV. SUMMARY AND CONCLUSIONS

We have presented the transient results of our numerical simulations of binary nucleation in vapor-to-liquid phase

transitions. These studies complement our earlier steady state analysis<sup>35</sup> and cover the same range of system parameters. For all of our systems we found that, at the earliest times, the cluster concentrations and the particle fluxes build up more quickly in the direction of the species with the higher impingement rate. The region with the highest flux then gradually shifts towards the saddle point, and during this part of the transient period (roughly for  $t < t^*$ ), it can extend over the ridge that lies between the saddle point and the pure component axis. During the latter part of the transient period, the particle flux through the saddle point grows rapidly and usually becomes predominant in steady state. When steady state nucleation occurs via ridge crossing, we have seen that it arises naturally as an arrested transient state. The region of highest flux simply appears to get stuck on its way to the saddle point. We also found that the ratio of nonequilibrium to equilibrium concentrations ( $\Phi$ ) has a quasi-universal behavior that is determined primarily by the thermodynamic properties of the liquid mixture. The relative sizes of the evaporation rate coefficients are the principal factors determining the qualitative appearance of the  $\Phi$  plots.

In addition to improving our qualitative understanding of transient binary nucleation, we quantitatively tested the available analytical expressions for the time lag of the saddle point nucleation flux. Both of these expressions overpredicted the numerically derived time lags under our conditions. Wilemski's expression,<sup>30</sup> however, gave better agreement with the numerical results than did that of Shi and Seinfeld.<sup>33</sup> We also noted that the theoretical behavior of the saddle point time lag may indicate when ridge crossing nucleation is the dominant steady state process, although we do not actually expect this behavior to be characteristic of the *observed* time lag when the major nucleation current avoids the saddle point.

## ACKNOWLEDGMENTS

G.W. thanks Bob Cook for helpful discussions. We also thank V. Shneidman for his comments on our manuscript. This work was supported by the National Science Foundation, Division of Chemistry under Grant No. CHE-9502604 (B.E.W.) and by the U.S. Department of Energy, Office of Basic Energy Sciences, Division of Geosciences and Engineering (G.W.). Part of this work was performed under the auspices of the U.S. Department of Energy by the Lawrence Livermore National Laboratory under Contract No. W-7405-ENG-48.

<sup>1</sup> V. A. Shneidman, Phys. Rev. Lett. **75**, 4634, (1995).

<sup>2</sup> K. F. Kelton, J. Non-Cryst. Solids **163**, 283 (1993).

<sup>3</sup> W. G. Courtney, J. Chem. Phys. **36**, 2009 (1962).

<sup>4</sup> R. P. Andres and M. Boudart, J. Chem Phys. **42**, 2057 (1965).

<sup>5</sup> L. R. Hile, Ph.D. thesis, Princeton University, 1969.

<sup>6</sup> F. F. Abraham, J. Chem Phys. **51**, 1632 (1969).

<sup>7</sup> H. L. Frisch and C. C. Carlier, J. Chem Phys. **54**, 4326 (1971).

<sup>8</sup> B. T. Draine and E. E. Salpeter, J. Chem. Phys. **67**, 2230 (1977).

<sup>9</sup> D. Peak, J. Chem. Phys. **68**, 821 (1978).

<sup>10</sup> K. F. Kelton, A. L. Greer, and C. V. Thompson, J. Chem. Phys. **79**, 6261 (1983).

<sup>11</sup> V. A. Shneidman, Sov. Phys. Tech. Phys. **32**, 76 (1987).

<sup>12</sup> H. Trinkaus and M. H. Yoo, Philos. Mag. A **55**, 269 (1987).

<sup>13</sup> A. Yu Klimenko, Izv. Akad. Nauk SSSR, Mekh. Zhidk. Gaza No. 1, 163 (1988) [Fluid Dynamics **23**, 135 (1988)].

<sup>14</sup> B. Shizgal and J. C. Barrett, J. Chem Phys. **91**, 6505 (1989).

<sup>15</sup> G. Shi, J. H. Seinfeld and K. Okuyama, Phys. Rev. A **41**, 2101 (1990).

<sup>16</sup> B. Nowakowski and E. Ruckenstein, J. Coll. Interface Sci. **145**, 182 (1991).

<sup>17</sup> V. A. Shneidman, Phys. Rev. A **44**, 2609 (1991).

<sup>18</sup> V. A. Shneidman and M. C. Weinberg, J. Chem. Phys. **95**, 9148 (1991).

<sup>19</sup> D. T. Wu, J. Chem. Phys. **97**, 2644 (1992).

<sup>20</sup> V. A. Shneidman and M. C. Weinberg, J. Chem. Phys. **97**, 3621 (1992).

<sup>21</sup> V. A. Shneidman and M. C. Weinberg, J. Chem. Phys. **97**, 3629 (1992).

<sup>22</sup> V. A. Shneidman, in *Nucleation and Atmospheric Aerosols*, edited by N. Fukuta and P. E. Wagner (Deepak, Hampton, 1992), p. 107.

<sup>23</sup> J. J. Hoyt and G. Sundar, Scripta Metall. Mater. **29**, 1535 (1993).

<sup>24</sup> L. Demeio and B. Shizgal, J. Chem. Phys. **98**, 5713 (1993).

<sup>25</sup> P. Demo and Z. Kožisek, Phys. Rev. B **48**, 3620 (1993).

<sup>26</sup> P. Demo and Z. Kožisek, Philos. Mag. B **70**, 49 (1994).

<sup>27</sup> G. Shao and P. Tsakiropoulos, Acta Metall. Mater. **42**, 2937 (1994).

<sup>28</sup> G. Sundar and J. J. Hoyt, J. Mater. Res. **10**, 1674 (1995).

<sup>29</sup> K. F. Kelton, Mat. Sci. Eng. B **32**, 145 (1995).

<sup>30</sup> G. Wilemski, J. Chem. Phys. **62**, 3772 (1975).

<sup>31</sup> F. J. Schelling and H. Reiss, J. Chem. Phys. **74**, 3527 (1981).

<sup>32</sup> F. J. Schelling and H. Reiss, J. Colloid Interface Sci. **83**, 246 (1981).

<sup>33</sup> G. Shi and J. H. Seinfeld, J. Chem. Phys. **93**, 9033 (1990).

<sup>34</sup> R. McGraw, J. Chem. Phys. **102**, 2098 (1995).

<sup>35</sup> B. E. Wyslouzil and G. Wilemski, J. Chem. Phys. **103**, 1137 (1995).

<sup>36</sup> K. Nishioka and K. Fujita, J. Chem. Phys. **100**, 532 (1994).

<sup>37</sup> Z. Kožisek and P. Demo, J. Cryst. Growth **132**, 491 (1993).

<sup>38</sup> Z. Kožisek and P. Demo, J. Chem. Phys. **102**, 7595 (1995).

<sup>39</sup> H. Reiss, J. Chem. Phys. **18**, 840 (1950).

<sup>40</sup> G. Wilemski and B. E. Wyslouzil, J. Chem. Phys. **103**, 1127 (1995).

<sup>41</sup> Even this critical flux occasionally overshoots its steady state value by a small amount. The absolute value in Eq. (7) prevents  $t^*$  from being underestimated.

<sup>42</sup> In the equation for  $\tan \alpha$  we have corrected a sign error in the formula given by Shi and Seinfeld. The error arises because  $D_{AB} < 0$ . With the correct sign,  $\alpha$  stays within the physically acceptable range  $0 \leq \alpha \leq \pi/2$ , which is especially important in the approach to unary nucleation.

<sup>43</sup> There is a sign error in the last term of the density fit for *o*-xylene given in Ref. 35. The correct expression is,  $\rho_{o-xylene} = 1.1101 - 0.6063(10^{-3})T - 0.1389(10^{-5})T^2 + 0.39376(10^{-8})T^3 - 0.43423(10^{-11})T^4$ .

<sup>44</sup> Strictly, it is the effective first order rate coefficients given by  $\Gamma_A(i,j)N_A$  and  $\Gamma_B(i,j)N_B$  that differ greatly as long as the mass accommodation coefficients are comparable.

<sup>45</sup> D. Stauffer, J. Aerosol Sci. **7**, 319 (1976).

<sup>46</sup> R. Strey and Y. Viisanen, J. Chem. Phys. **99**, 4693 (1993).

<sup>47</sup> W. J. Shugard, R. H. Heist, and H. Reiss, J. Chem. Phys. **61**, 5298 (1974).

<sup>48</sup> K. Suzuki and V. A. Mohnen, J. Aerosol Sci. **12**, 61 (1981).

<sup>49</sup> V. A. Shneidman (private communication, 1996).

<sup>50</sup> V. A. Shneidman, Sov. Phys. Tech. Phys. **33**, 1338 (1988).

<sup>51</sup> The parabolic approximation is actually used in different ways to obtain  $\lambda_{SS}$  and  $L(w^*, n^*)$ . To find the time dependent cluster concentrations that ultimately determine  $\lambda_{SS}$ , Shi and Seinfeld solved an approximate partial differential equation whose form is strongly influenced by the quadratic expansion of  $W$ . To obtain Eq. (8d), the quadratic expansion of  $W$  is used only to simplify the evaluation of the integrals that define  $L(w^*, n^*)$ . The numerical consequences of these two approaches differ appreciably.